

New Method for Determining Azimuths of ELF Signals Associated with the Global Thunderstorm Activity and the Hunga Tonga Volcano Eruption

J. Kubisz¹, M. Golkowski², J. Mlynarczyk³, M. Ostrowski^{1†}, A. Michalec^{1†}

¹ Astronomical Observatory, Jagiellonian University, Kraków, Poland.

² Department of Electrical Engineering, University of Colorado Denver, Denver, USA.

³ Institute of Electronics, AGH University of Science and Technology, Kraków, Poland.

Corresponding author: Michał Ostrowski (michal.ostrowski@uj.edu.pl)

† Emeritus.

Key Points:

- A new method for deriving wave arrival azimuths with parametric temporal filtering of electromagnetic waves in the ELF band is introduced.
- A multitude of thunderstorms on Earth varying during the day at different azimuths are resolved.
- The Hunga Tonga volcano eruption signals are diffracted by $\approx 10^\circ$ when propagating in the Earth-ionosphere cavity over the polar regions.

Abstract

A new method is proposed for deriving Extremely Low Frequency (ELF) wave arrival azimuths using the wide range of signal amplitudes, contrary to previously applied high amplitude impulses only. The method is applied to observations from our new magnetic sensor in the Hylaty station with an 18 bit dynamic range and a 3 kHz sampling frequency. We analyzed a day of January 15th, 2022, to test the procedure against the ability to extract ELF signals generated during the Hunga Tonga volcano eruption. With complementary filtering of power line 50 Hz signatures, precise azimuth information can be extracted for waves from a multitude of thunderstorms on Earth varying during the day at different azimuths. A phenomenon of successive regular variation - decay or activation - of thunderstorms activity with varying azimuth is observed, possibly due to passing over the solar (day/night) terminator, and signatures of azimuth direction change during this passage can be noted. We also show that the erupting Hunga Tonga volcano associated impulses dispersed due to a long propagation path are clearly revealed in the azimuth distribution with analysis using parameters fitted to measure slowly varying signals, but not for fast varying impulses. We show that the Hunga Tonga related signals arrive from the azimuth $\approx 10^\circ$ smaller than the geographic great circle path. The

35 discrepancy is believed to be due to propagation through the polar region and in the vicinity of the
36 solar terminator.

37 **1. Introduction**

38

39 Electromagnetic fluctuations in the extremely low frequency (ELF) band, defined here as 0.03 – 1000
40 Hz, provide a unique source of geophysical information that has not been exploited in depth
41 (*Nickolaenko, 1997; Price, 2016; Nickolaenko et al., 2002*). Naturally occurring ELF waves include
42 Schumann resonances and ELF transients created by lightning, with often associated optical
43 phenomena of sprites and elves. These waves are transmitted in the Earth-ionosphere waveguide and
44 therefore provide a diagnostic on the lower ionosphere, which itself responds to solar changes and
45 space weather phenomena (*Golkowski et al., 2018*). Ground based ELF observations have also become
46 important support in identification of gravitational waves (*Coughlin et al., 2018*).

47 Determining the arrival direction of natural emissions in the ELF/VLF bands has been of
48 longstanding interest and is possible from a single receiver station if two or more components of the
49 propagating fields are observed (*Kemp, 1971; Jones and Kemp, 1970; Kemp and Jones, 1971*). In the
50 VLF band, the multimodal aspect of propagation in the Earth-ionosphere waveguide can yield
51 polarization error in direction finding, which means signals are often analyzed in the frequency
52 domain and efforts are made to quantify the polarization (*Golkowski and Inan, 2008; Hosseini et al.,*
53 *2018*). In lightning detection networks such as the Vaisala GLD360 system, azimuth of VLF transients
54 is determined in the time domain and polarization errors are mitigated by using only the first 200 μsec
55 of the lightning signal (*Said et al., 2010*).

56 In the ELF band the propagation is unimodal and typically two orthogonal measurements of
57 the horizontal magnetic field are employed to find the arrival angle (*Nieckarz et al., 2011; Füllekrug*
58 *and Constable, 2000*). Nevertheless, there can be errors in the emission source direction finding at
59 ELF claimed to be due to anisotropy of the ionosphere (*Füllekrug and Sukhorukov, 1999*) and
60 scattering from the sharp conductivity boundaries such as ocean/land boundaries and the solar
61 (day/night) terminator (*Mlynarczyk et al., 2017; Nickolaenko et al. 2018, 2021; Schvets et al. 2022*).
62 The impact of the ionospheric anisotropy on the signal propagation was discussed by *Nickolaenko and*
63 *Sentman (2007)* to be observed as characteristic variations of signal ellipticity with the frequency.
64 Techniques has been developed which seek to use two components of horizontal magnetic field and a
65 vertical electric field to improve accuracy (*Jones and Kemp, 1970; Kemp and Jones, 1971*). In all
66 cases of direction finding, operating over a larger bandwidth is known to reduce error (*Strangeways*
67 *and Rycroft, 1980; Mlynarczyk et al., 2017; Wood and Inan, 2002, 2004*).

68 As described in more detail below, the novelty of the present approach is the use of a
69 difference technique that intrinsically introduces selective temporal filtering that can be used to
70 remove power line interference or target specific temporal signatures. Thus a significant amount of the
71 measurement data can be applied for the azimuth determinations, contrary to previous studies focusing
72 on large ELF impulses in the data (see, e.g., a recent description in *Nickolaenko et al. 2023*) For

73 illustration of the possibilities of the proposed novel approach, we analyze observations from the day
 74 of January 15th, 2022, when occurrence of the Hunga Tonga (HT) volcano eruption created a strong
 75 compact ELF source (*Nickolaenko et al., 2022; Mezentsev et al., 2022; Bor et al., 2023; see also*
 76 *Nickolaenko et al., 2023*). We also present the capabilities of single site monitoring of global
 77 thunderstorm activity. In particular, at the figures one can note daily variations of the global
 78 thunderstorm activity, influenced by the Asian center at the azimuths $\sim 90^\circ$, operating in the hours 6 -
 79 10 h UT, shifting to the more powerful African center at the azimuths $\sim 180^\circ$ (12 - 18 h UT), and
 80 shifting toward the South American center at the azimuths $\sim -90^\circ$ (18 - 22 h UT). The derived azimuths
 81 can be compared in detail with the list of selected reference azimuths from the Hylaty station
 82 presented in the Table 1. When inspecting the figures below one should not forget that the presented
 83 azimuth structures are significantly "filtered" by the parameters' sets selected in the applied azimuth
 84 derivation and the procedure provides more or less symmetric distribution for the source azimuth + or
 85 -180° .

86

87 Table 1. A list of selected reference geographic azimuths A, their respective anti-azimuths (indicated
 88 with an asterisk) and distances from the Hylaty ELF station.

89

Place	A [°] ($0^\circ < A < 180^\circ$)	A [°] ($-180^\circ < A < 0^\circ$)	Distance [Mm]
Hawaii, Honolulu	0.4	-179.6 *	12.2
Angola, Lubango	9.6 *	-170.4	7.2
Nigeria, Lagos	27.5 *	-152.5	5.1
Hunga Tonga	32.9	-147.1 *	16.4
Alps, Graz	38.4 *	-111.6	0.6
Japan, Honshu	48.4	-131.6 *	8.6
Russia, Moscow	48.7	-131.3 *	1.3
Guinea Bissau	52.8 *	-127.2	5.4
Brazil, Belem	57.6 *	-122.4	7.4
Uruguay, Montevideo	58.4 *	-121.6	12.1
Brazil, Recife	59.3 *	-120.7	8.4
Papua New Guinea, Port Moresby	68.7	-111.3 *	13.3
Hong Kong	73.8	-106.2 *	8.3
Philippines, Manila	74.1	-105.9 *	9.4
Alps, Chamonix	78.6 *	-101.4	1.2
Vietnam, Hanoi	80.6	-99.4 *	7.8
Portugal, Porto	81.6 *	-98.4	2.6
Brazil, Manaus (Amazon region)	82.3 *	-97.7	9.7
Borneo	88.9	-91.1 *	10.1
Bangladesh, Dhaka	89.8	-90.2 *	6.4
Indonesia, Jakarta	98.3	-81.7 *	10.1
Haiti, Port-au-Prince	102.8 *	-77.2	8.8
India, Mumbai	108.4	-71.6 *	5.6
Pakistan, Karachi	108.7	-71.3 *	4.7
US, Florida, Orlando	118.9 *	-61.1	8.6

Nicaragua, Managua	121.2 *	-67.9	10.3
US, Georgia, Atlanta	124.5 *	-55.5	8.3
Madagascar	155.1	-24.9 *	8.0
Kenya, Mombasa	159.0	-21.0 *	6.1
DR Kongo, Kisangani	176.4	-3.6 *	5.4

90

91

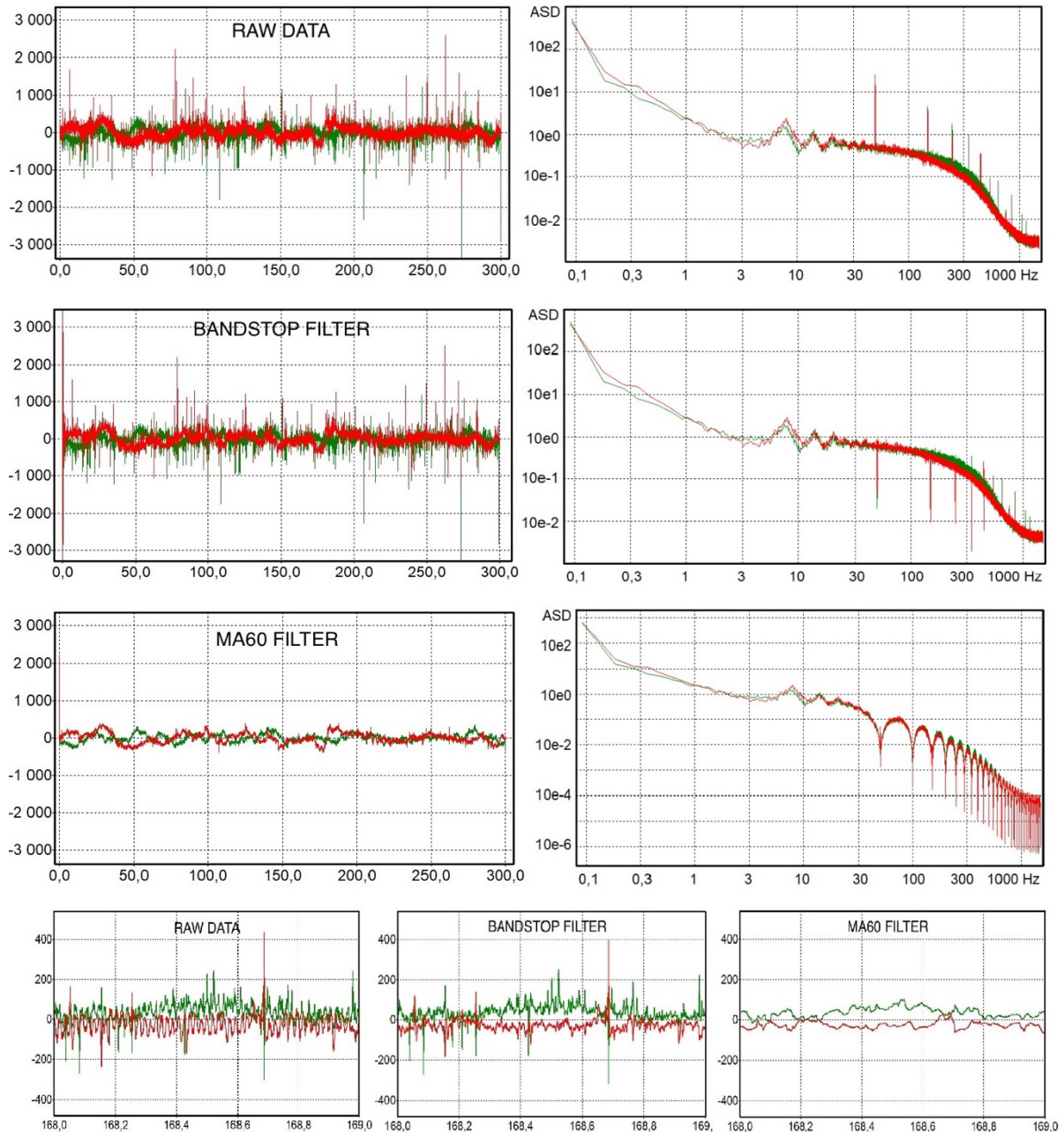
92 **2. ELA11 magnetic sensor**

93

94 We use data (a data copy available at DATA_HYLATY_ELA11_2022_01_15, 2022) from our novel
 95 magnetic sensor ELA11 (Mlynarczyk et al., in preparation) with two perpendicular, NS and EW, active
 96 antennas installed at the Hylaty station (49.2° N, 22.5° E). The new sensor has a high 18-bit ADC
 97 resolution, enabling a much higher dynamic range than our ELA10 sensors deployed in the WERA
 98 system (Kulak et al., 2014; <https://www.ou.edu.pl/WERA>). It also features a sampling frequency of
 99 3 kHz (3004.81 Hz precisely), which is over three times higher than that of the ELA10 sensor. The
 100 increased dynamic range and higher bandwidth, as well as use of a Bessel anti-aliasing filter, enable
 101 improved resolution of individual impulses in the registered signal and better characterization of the
 102 temporal signal shape, as illustrated in Figure 1. The measured signal is provided by natural numbers
 103 in the ELA11 sensor units, with 1 pT magnetic field change equivalent to 12.68 sensor units. When
 104 analyzing the measured signal variations, one should keep in mind that the presented data have a zero
 105 reference point near the middle of the measurement range and only presented magnetic field variations
 106 have physical meaning.

107 The data analyzed in the present paper are available from an on-line repository (Kubisz 2023).

108



109
110

111 Figure 1. **A** (two panels at the top): An example 300 s (5 minutes') data stream in the receiver units
 112 and the associated log-log Amplitude Spectrum Density [pT / SQRT(Hz)] in NS (red) and EW
 113 (green) antennas from January 15th, 2022, 0:00-0:05 UT, from the ELA11 magnetometer at the Hylaty
 114 station; the same data and respective spectra are presented after electric power line filtering (see Sect.
 115 3) with the bandstop filter (**B**, second row) and with the MA60 filter (**C**, third row); **D** (bottom):
 116 Detailed data comparison for a short 1 s range of unfiltered data (left panel) and filtered data with both
 117 the bandstop filter (middle panel) and the MA60 filter (right panel). Please, note different vertical
 118 scales at the presented spectra.

119

120 3. Derivation of ELF signal azimuths

121

122 Let us consider a geographic azimuth A measured from the North toward the East direction and we
 123 assume that the studied ELF waves have magnetic field component parallel to the Earth surface. We
 124 derive the signal azimuth of arrival, A_i , using the registered signal changes in our NS and EW antennas
 125 between time instants t_i and t_{i+n} from the expression:

126

$$127 \tan(A_{(i, n)}) = - \Delta B_{NS(i, n)} / \Delta B_{EW(i, n)} \quad (1)$$

128

129 where $\Delta B_{(i, n)} = B_{(i+n)} - B_{(i)}$ is a difference between two signal measurements from a given magnetic
 130 antenna, NS or EW. Let us stress that the sign "minus" in the above expression is required due to our
 131 use of the measured ΔB_{EW} , not ΔB_{WE} . As pointed out above, the parameter n provides the time delay
 132 between successive signal samples applied for the azimuth derivation. For example, $n=1$ corresponds
 133 to two successive samples in the 3 kHz measurements, $n=60$ corresponds to a delay of 0.02 s, the
 134 50Hz electric power line period, and $n=3000$ to a delay of 1 second. Depending on positive or
 135 negative values of the derived $\Delta B_{(i, n)}$ we obtain the azimuths in the range $(-180^\circ, +180^\circ)$. One should
 136 stress that for a single impulse the proposed approach – applying signal changes between two selected
 137 measurements instead of the full impulse amplitude – results in two azimuth values, A and $A \pm 180^\circ$,
 138 derived respectively for its growing part and declining part. Below, we apply this procedure to all
 139 successive measurements within the analyzed time range, applying the selected time delay n at each
 140 "i".

141 In the applied digital electronics, the measurement values are given by natural numbers, and
 142 with the applied 3 kHz sampling frequency, the derived differences between successive samples ΔB
 143 are often represented by small natural numbers or even zero. Such small values in the numerator or
 144 denominator of the right-hand side of Eq. (1) can drive the inverse tangent function to significant
 145 maxima of derived azimuth distributions at $(\pm) 0, 90^\circ$ and 180° degrees, as well as several discrete
 146 values $90^\circ \cdot (j/k)$, where j and k are small natural numbers. Additionally, the electric power grid
 147 associated signal at 50 Hz (see Figure 1) can introduce large scatter in the derived azimuth distribution
 148 and its possible arrangement respective to local electric power lines. Thus, when selecting signals for
 149 the azimuth derivation, we limit their magnitudes to pre-defined values for any given n by selecting
 150 the minimum and maximum limits r_{\min} and r_{\max} for the signal change parameter $r =$
 151 $\text{SQRT}(\Delta B_{EW}^2 + \Delta B_{NS}^2)$. Depending on the selected minimum and maximum values of this parameter
 152 one can study azimuth values for different wave (impulse) amplitudes, using the full available data
 153 above the level of electric power line signal variations, but not restricted to large individual magnetic
 154 peaks only. One should remember that the proposed procedure generates azimuth values differing by
 155 180° between the rising and falling parts of the individual impulse. The analogous azimuth changes

156 would be obtained for positive and negative discharges as well as for signals propagating directly from
157 the discharge location to the measuring station and the one reaching the station after propagation by
158 the longer path around the Earth. Thus, in the presented figures we use an azimuth scale from -180° to
159 $+180^\circ$ to present data resulting from Eq. 1, with expected symmetric A and $A\pm 180^\circ$ values generated in
160 this range by any single lightning generated impulse within the measurement range $r_{\min} < r < r_{\max}$. An
161 inspection of the derived azimuth distributions in the figures below reveals a clearly visible difference
162 between positive and negative azimuth distributions pointing to the existence of numerous temporally
163 asymmetric signals with some superimposed background fluctuations and possible deviations of the
164 impulse path from the geographic great circle.

165 The raw unfiltered data has a strong signature of the local electric power line at 50 Hz, which
166 makes azimuth determination more difficult for small impulses. Specifically, from a visual inspection
167 of the raw data (see Fig. 1D) we find that r values below $r_{50\text{Hz}} \sim 100$ (or ~ 8 pT in physical units) are not
168 usable for the azimuth derivation when processing our raw data. To get around this limitation, we
169 propose two optional approaches to extract azimuth information from the low amplitude signal
170 fluctuations:

171 — by selecting the electric grid frequency $n=60$ (or its multiples) in Eq. 1 one removes significant part
172 of the electric power line perturbations in the analysis (cf. Mitchell 1976) by using measurements in
173 the same phase of this perturbing signal. However, the existing irregularities in the electric network
174 signal shapes (see Figure 1D) still leave a noticeable scatter in the derived azimuths, and of course we
175 lose the freedom to use different values of n in the analysis. Below, we positively tested the validity of
176 such an approach (called also an *inter-period subtraction*) by comparing the azimuth distributions
177 derived with small $r_{\max} < r_{50\text{Hz}}$ with the ones for the larger impulses above the electric grid
178 fluctuations.

179 — by filtering the 50 Hz component and its harmonics from the data one removes a significant part of
180 its contribution to the analyzed signal. The situation is more complicated however, because the power
181 line signal is subject to various fluctuations and any filtering procedure also perturbs the background
182 ELF noise to be analyzed. Thus, it is essential to carefully evaluate possible 50 Hz filtering impact on
183 the derived azimuths, which may significantly vary depending on the filtering method and the n , r_{\min}
184 and r_{\max} parameters selected in the analysis. Below we will discuss application of two significantly
185 different filtering procedures.

186 The first approach uses a third-order bandstop Butterworth filter (henceforth: “the bandstop
187 filter”) which enables removal of the 50 Hz line fluctuations and its harmonic frequencies if they have
188 significant amplitudes. A great advantage of a software filter over a hardware filter is that its center
189 frequency and bandwidth can be adjusted to the processed signal, to minimize the distortions (see, e.g.
190 Mlynarczyk et al. 2017). For studying short data samples (like the 5-minute or shorter time samples
191 considered in our measurements) or individual strong impulses we typically use a filter with a

192 bandwidth of only 0.3 Hz at 50 Hz and 150 Hz (the precise central frequency is measured for each
193 date file). Since the filter bandwidth is very narrow, it has little influence on the amplitude of lightning
194 associated impulses. If 250 Hz and higher harmonic frequencies have a significant amplitude, one can
195 filter them as well, but it is rarely necessary. The filter bandwidth at these higher harmonic frequencies
196 is a little larger (we increment it by 0.2 Hz at each consecutive harmonic frequency). A slightly less
197 intricate application of this filter is applied below where we analyze long 24h measurements, with
198 present significant variations of the 50 Hz line: its intensity and central frequency, as well as the line
199 width and more extended low intensity wings. For such cases we decided to use a uniform in all
200 measurements, wider filter bandwidth of 1 Hz at the 50 Hz line as well as at its all registered harmonic
201 frequencies. Thus, small observed variations of the line central frequency do not influence the
202 filtering, but we note that the 50 Hz line wings as measured at our site sometimes extend off the
203 applied 1 Hz exclusion bandwidth. Therefore, the remaining signal from the wings can still be left in
204 the data after filtering, possibly perturbing low amplitude wave measurements. The raw ELA11 data
205 are compared with the filtered data resulting from application of the above-described filter in Figure
206 1B and D.

207 A significantly different, second filtering procedure uses the moving average (MA60) filter,
208 perhaps one of the most widely used FIR filters, here with averaging over the electric grid period of
209 0.02 s (i.e. over 60 successive measurement points). The filter fully removes the 50 Hz line and all its
210 higher harmonic frequencies up to the considered here upper limit of 1500 Hz. In this case the
211 procedure provides a low band pass filtering, significantly damping high frequency impulses, but
212 preserving relatively undisturbed the low frequency ELF fluctuations. To see the effect, our raw data
213 are compared below with the filtered ones in Figure 1C and D, showing that besides the 50 Hz
214 periodic signal the filtering procedure removes (or significantly damps) all naturally occurring strong
215 spikes.

216 Thus, when applying any of these 50 Hz filtering procedures, or not applying filtering at all,
217 one should be careful in interpretation of the azimuths derived from the respective data for any set of
218 the analysis parameters r_{\min} , r_{\max} and n . When possible, e.g., from a nearby/strong thunderstorms, one
219 can compare the derived signal azimuth distributions with the one derived from the large impulses at
220 $r > r_{50\text{Hz}}$. Also, the azimuth continuity of the signal from a single thunderstorm center, with its
221 expected varying daily intensity and scatter, confirm reality and characterize accuracy of the measured
222 azimuths. The studies, without considering powerful sources of ELF electromagnetic waves with
223 known location (like the volcano eruption) or impulses from individual discharges registered in the
224 VLF networks (e.g., WWLN or Vaisala) are not suitable to directly extract information about eventual
225 systematic wave diffraction and respective azimuth modification along the signal path in the Earth-
226 ionosphere cavity. However, such extended detailed analysis, involving studies of EM impulses from

227 individual lightning discharges registered by the WWLLN VLF network, lays outside the scope of the
228 present paper, with exception of the signal azimuth verification for the Hunga Tonga volcano eruption.

229 One should note that the applied filtering procedures introduce unphysical perturbed signal in
230 the very beginning of each filtered 300s data stream. Therefore, in this work we simply removed the
231 initial 2.6s of the data where such artifacts are observed from all analyzed filtered data samples.

232 Another option that one can use is to append the last part of the previous data file to the data range for
233 filtering and removing it afterwards.

234

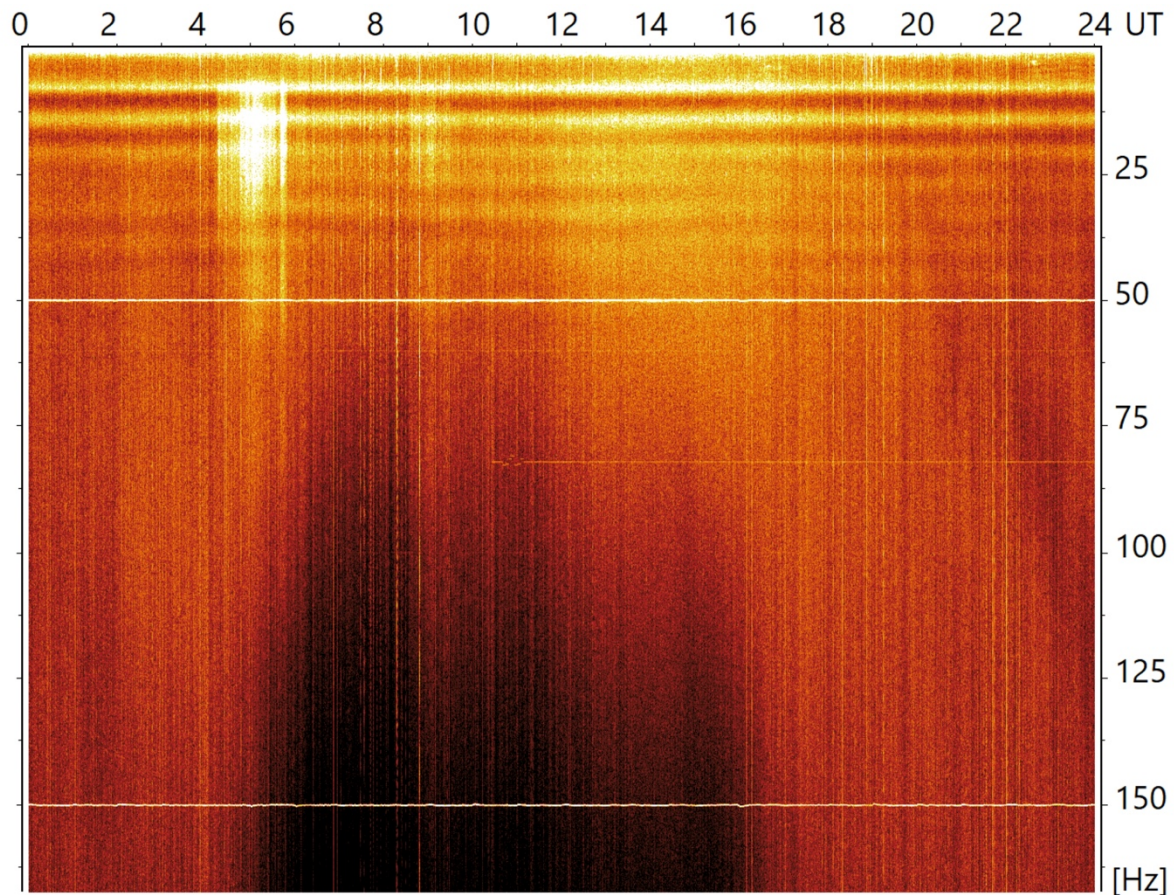
235 **4. Azimuths of ELF electromagnetic waves registered in the Hylaty station**

236

237 To illustrate the range of possibilities of the proposed ELF signal azimuth analysis applied to the
238 ELA11 receiver measurements we selected the day of January 15th, 2022 (0-24 h UT). We processed
239 the data to extract information on natural ELF wave fields anisotropies and additionally, to check
240 constraints on revealing the ELF signature associated with the HT volcano eruption (*Nickolaenko et*
241 *al.*, 2022; *Bor et al.*, 2023). The eruption signatures in the time range 4:15-5:50 UT for the main
242 eruption and in the time range 8:35-9:30 UT for the next weaker one, are visible in our data, as
243 presented in the 24-hour dynamic spectrum evolution at Figure 2. The discussed below azimuth
244 distributions provide an additional tool to extract the HT electromagnetic signal from a background
245 thunderstorms' noise superimposed in the plot.

246 Before inspecting the daily evolution of spectrum and azimuth let us explain that to reveal
247 variations in all considered frequency and amplitude ranges we performed fine tuning of the presented
248 values to the plot color scale by using two numerical factors, the first was multiplying the data while
249 the second was subtracted from the data. Thus, in Figure 2 one can analyze nearly all spectra in the full
250 range of 1-165 Hz, clearly revealing also the secondary HT eruption signatures, on the expense that
251 strong HT signal is presented as white, being unresolved above the applied color scale.

252



253
254

255 Figure 2. Evolution of the ELF signal power spectrum in the EW antenna on January 15th, 2022, from
256 0 till 24 UT. Each vertical line shows a successive 75-second spectrum in the frequency range up to
257 165 Hz. We used the Hann window in computations to minimize nearby thunderstorms' noise in the
258 plot. The HT eruption signatures are clearly visible for frequencies less than 50 Hz at 4:15-5:50 UT
259 and a somewhat weaker eruption from 8:35 till 9:30 UT.

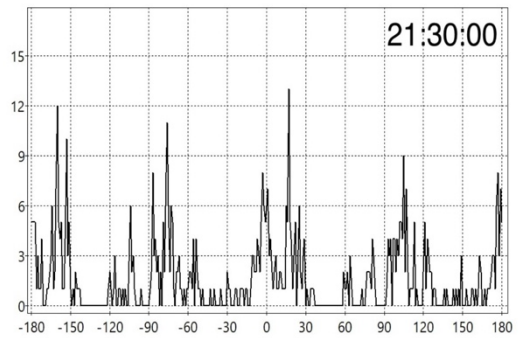
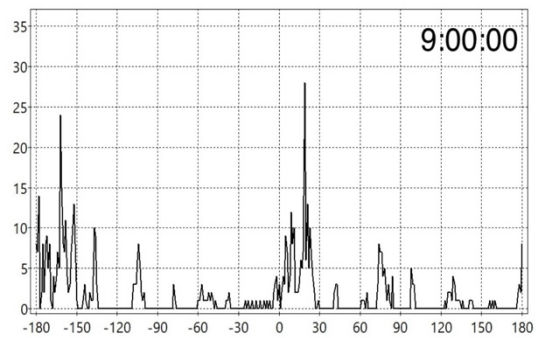
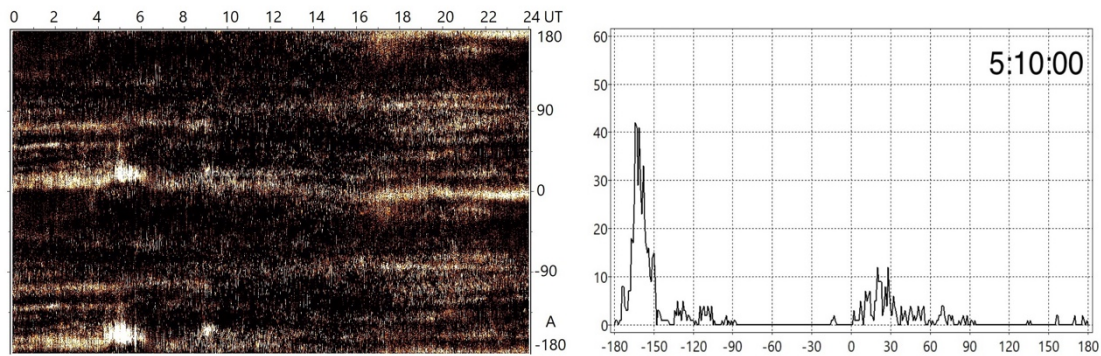
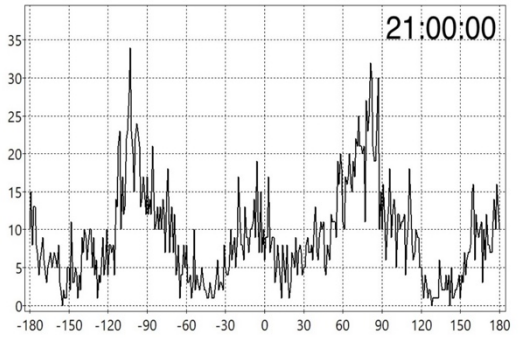
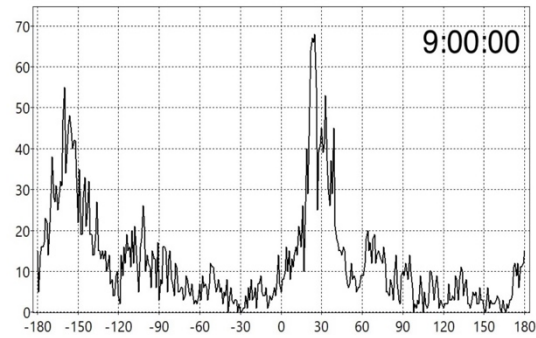
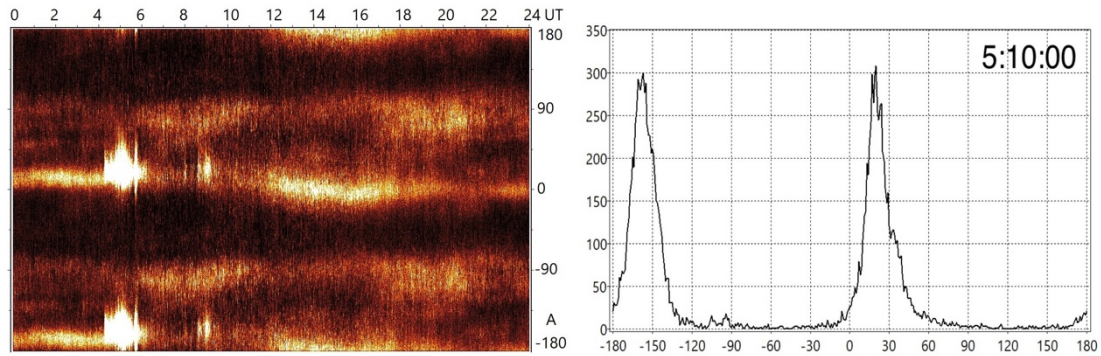
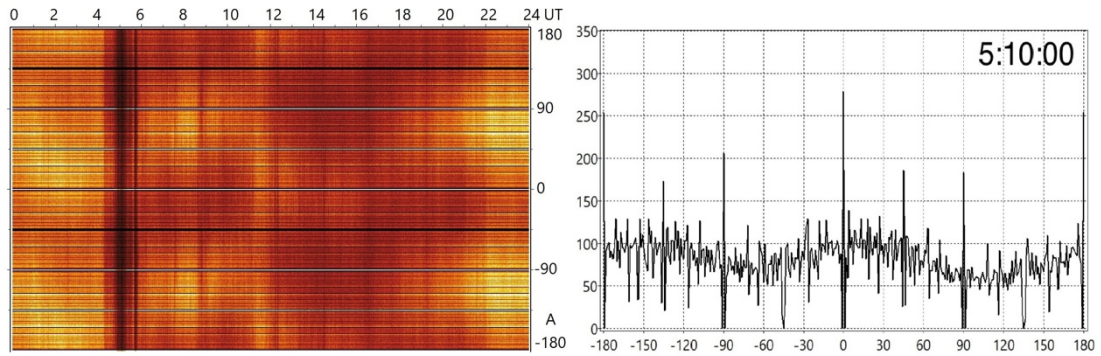
260

261 In Figure 2 one can note continuous horizontal stripes of at least seven Schumann resonances,
262 a 50 Hz power line, and its harmonic at 150 Hz, also a weak 60 Hz line and the 82 Hz (possibly a
263 Russian submarine communication) line switching on at 10 UT. One can also notice a decrease in
264 power of higher frequency components in the spectra (steepening of the spectrum) from approximately
265 5 till 16 UT (darker colors at higher frequencies). Strong succession of impulsive signals generated
266 during the HT main eruption occurs during the HT primary eruption and again but slightly less
267 pronounced during the secondary. The analogous, but less pronounced HT related features are also
268 visible in the (not presented) power spectrum evolution plot for the NS antenna, as expected for the
269 HT azimuth (see below).

270

271 Now, let us analyze a daily (Jan. 15th, 2022) evolution of ELF signal azimuths derived as
272 explained above in Section 3. One should remember that differences of the considered source
distances lead to modification of intensity and dispersion of individual impulses. Below, we

273 demonstrate how selection of parameters n , r_{\min} and r_{\max} enables one to extract azimuths for particular
274 ELF signals and thunderstorm regions. In the plots, we originally searched for signatures of the HT
275 eruption near its geographic azimuth $A_{\text{HT}} = 32.8^\circ$ and $A_{\text{HT}} - 180^\circ = -147.2^\circ$ to learn that it is significantly
276 shifted to $\approx 20^\circ$ and -160° , respectively. The distance to the erupting volcano is significant, $D = 16400$
277 km, so we expected and confirmed in the measurements below that the volcano originated signals are
278 subject to significant dispersion even for the direct path propagation.
279



281
 282 Figure 3. Azimuth daily evolution and distributions of derived azimuths during 75 s time bins
 283 beginning in selected times, derived with the raw data for $n=60$. We present plots for **A** (two panels at
 284 the top) ($r_{\min}=10$, $r_{\max}=30$) and 5:10:00 UT; **B** (4 panels in rows 2 and 3) ($r_{\min}=200$, $r_{\max}=300$) and
 285 5:10:00 UT, 9:00:00 UT and 21:00:00 UT; and **C** (4 panels at the bottom, rows 4 and 5) ($r_{\min}=500$,
 286 $r_{\max}=5000$) and 5:10:00 UT, 9:00:00 UT and 21:30 UT. At vertical axes of the azimuth distributions,
 287 we present the number of measurements per one-degree azimuth range. Note vertical scale changes
 288 between the presented azimuth distribution plots.

289

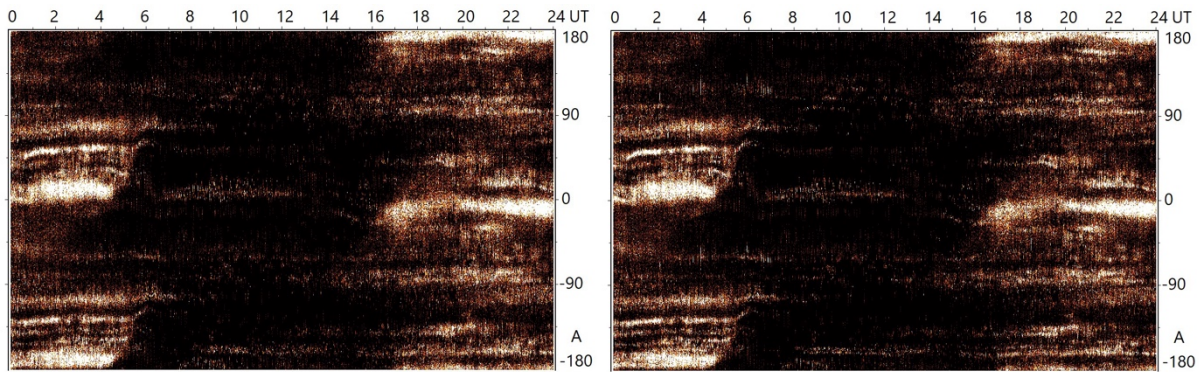
290 Let us start with the raw unfiltered data. Here to subtract the 50 Hz line contribution from the
 291 data we either select $n=60$ ($\Delta t_{50\text{Hz}} = 0.02$ s) to compare ELF signal changes in the same phase of the
 292 electric power line signal or we select only high amplitude ($r > r_{50\text{Hz}}$) impulses/waves for any selected
 293 n . When analyzing the results in the first considered case for $n=60$ we see that preferential values of r
 294 are comparable or above the electric line fluctuations, as the tests with $r_{\max} < r_{50\text{Hz}}$ show a significant
 295 random smoothing of the azimuth distribution as seen in Figure 3A. In a period of the high intensity
 296 HT eruption most of r measurements for $n=60$ are above r_{\max} selected for this plot and thus excluded
 297 from the plot, leading to a vertical dip in the azimuth distribution measurement (cf. Mezentsev et al.,
 298 2022). On the other hand, a clear HT signal dominating the azimuth distribution during the eruption
 299 (4:15 – 5:50 UT and near 9:00 UT) is visible in Figure 3B, where results for r a few times larger than
 300 $r_{50\text{Hz}}$ (still with $n=60$) are presented. Outside of the eruption times, the thunderstorm activity produces
 301 in this analysis quite diffuse, not well resolved structures. To reach high directional resolution of the
 302 incoming waves one must select $r_{\min} \gg r_{50\text{Hz}}$, as presented in Figure 2C. Then, both the HT primary
 303 and secondary eruption signatures are clearly visible, but also several separate azimuth ranges of
 304 thunderstorm activity, varying during the day, can be clearly resolved outside the HT eruption periods.
 305 In conclusion, use of $n=60$ to subtract the electric grid background seems to be fully effective only for
 306 large amplitude signals, while irregularities of the electric grid signal presented in Figure 1D (left plot)
 307 introduce significant scatter in azimuths derivations for smaller r .

308 From inspection of Figures 3B and C one should note, however, that the mean measured HT
 309 signal azimuth from our Hylaty ELF station appears to be near 20° , which is more than 10 degrees
 310 smaller than the HT geographic azimuth, $A_{\text{HT}} = 32.8^\circ$. An azimuthal deviation of similar magnitude
 311 from the true geographic azimuth for ELF measurements was also noted by Füllekrug and Sukhorukov
 312 (1999) to occur when the waves propagated near the high conductivity of the Pacific Ocean.
 313 Mlynarczyk et al. (2017) found that azimuthal deviations can be caused by diffraction from the solar
 314 terminator nonuniformity. Following those past studies, we interpret the presently measured difference
 315 as resulting from the signal deflection at ionospheric nonuniformities in the northern and southern
 316 polar regions as well as at the solar terminator. In this context it is worthy to note that the terminator

317 was passing over the Hylaty station in time of the volcano main eruption and the HT signal direct path
 318 to the station was close to the terminator in the polar region. In principle, also a contribution from the
 319 powerful African thunderstorm center at $A < 20^\circ$ could contribute to this distribution shift, but we note a
 320 fortunate significant calming of this signal (see Figure 4 and Figure 5 below) in the beginning of the
 321 HT eruptive activity what makes such an explanation doubtful.

322 One can also minimize the influence of electric grid signal at the derived azimuth distribution
 323 at any other selected n by considering values of r much higher than the ones in the grid signal. One
 324 should note here that a change of the grid signal from its minimum to maximum occurs at a time scale
 325 of $\frac{1}{4} \Delta t_{50\text{Hz}}$ (or $n=15$) and thus effective grid signal variations for $n < 15$ may be significantly smaller
 326 than the full amplitude $r_{50\text{Hz}}$. Thus, let us consider the case with $n=3$ (a time step of 1 ms) and the
 327 required large signal changes with $r_{\text{min}}=300$. At the resulting azimuth distribution presented on Figure
 328 4 one can note quite efficient azimuth resolution in the plot. However, we also note that the HT signal
 329 signature completely disappears from the plot. In fact, such an effect is expected for signals from a
 330 distant source since the impulses diminish their amplitudes and experience significant dispersion
 331 during propagation, contributing to the ELF signal with smaller r , outside the parameter range selected
 332 for this derivation. Removal of the HT contribution from the azimuth distribution reveals interesting
 333 structures on the remaining plot. In the analyzed winter day, a significant $\sim 12\text{h}$ range of low
 334 thunderstorm activity appears on the plot, between ca. 5 UT and 16:30 UT for thunderstorm centers
 335 close to azimuths 0° and $\pm 180^\circ$, while regularly shifting with time for growing azimuths, with the
 336 quiescence range roughly 6 UT–18 UT at 45° but extending only up to ~ 14 UT at the azimuth stripe
 337 visible above 90° . Following earlier publications we interpret this regular structure in the studied
 338 winter day at the Northern hemisphere as switching-off of the thunderstorm activity at successive
 339 azimuths by the propagating solar terminator. A similar but somewhat less regular process of azimuth
 340 dependent switching-on of the thunderstorm activity appears in the evening (see also Figure 5 below).
 341 Let us also note that careful inspection (also in the studies of filtered data below) of the considered
 342 thunderstorm switching-off ranges suggest existence of small upturns to higher azimuths before the
 343 quiescence phase (cf. Shvets et al. 2022). If real, such behavior could indicate the effect of the signal
 344 diffraction at the terminator passing over the given thunderstorm site. One more important feature is
 345 present in these azimuth data with absent HT signatures. An active thunderstorm center with the
 346 measured azimuth close to $A_{\text{HT}}=32.8^\circ$ (and -147.2°) initiated its activity before the HT main eruption
 347 (Figure 4B) and was continuing activity during the main eruption phase, as we observed in the
 348 respective azimuth distributions before and during the main eruption. Thus, it is important to know
 349 that this signal from the HT geographic azimuth is not the volcano eruption signature, but a
 350 superimposed thunderstorm activity.

351



352

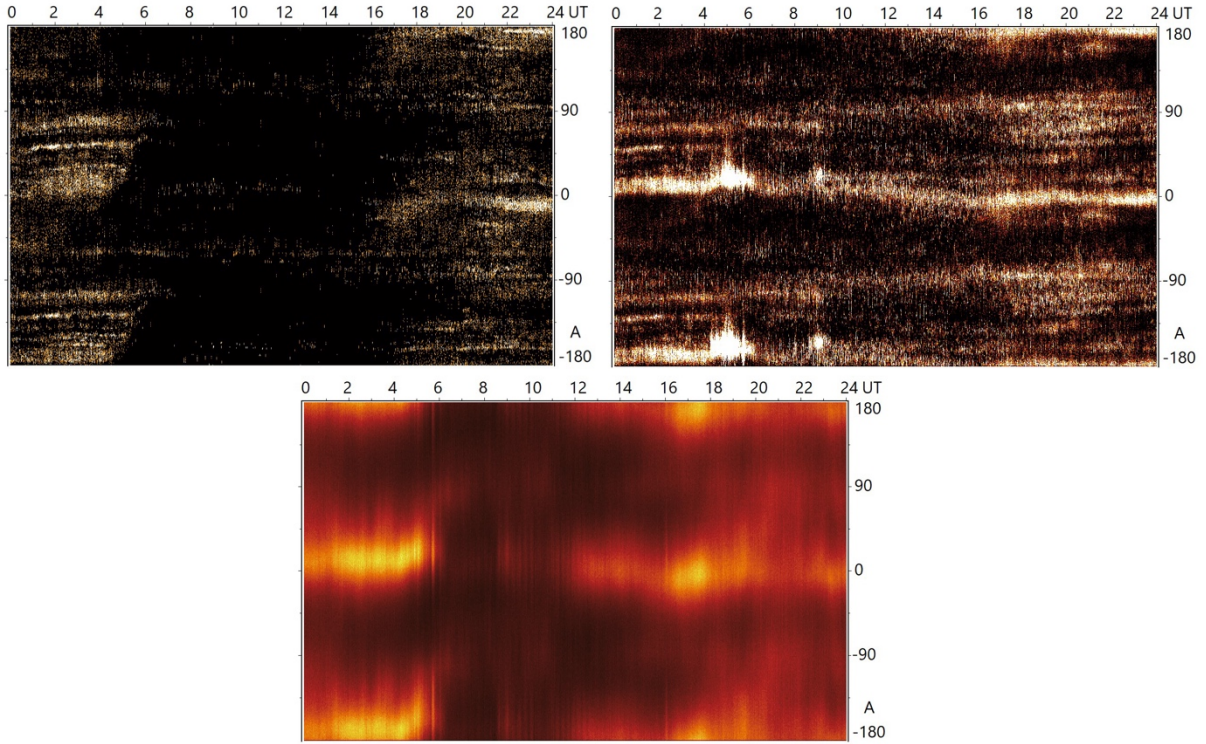
353 Figure 4. Comparing daily ELF signal azimuth distributions derived with $n=3$, $r_{\min}=300$ and $r_{\max}=3000$
 354 for **A.** the raw data (left); and **B.** the data with 50 Hz line filtered using the bandstop filter (right).

355 Existing slight differences between the plots are hardly visible.

356

357 Now, let us consider another suggested option for removing effects of 50 Hz line fluctuations
 358 from the analysis by removing the power line periodic signal and its harmonics with filtering
 359 procedures discussed in Section 3. Let us start with applying the bandstop filter. The resulting daily
 360 varying distribution of signal azimuths derived from such filtered data is presented in Figure 4B,
 361 where we selected for presentation quickly varying high amplitude impulses analyzed with $r_{\min}=300$
 362 and $n=3$. In this case the filtering procedure allows for tiny but visible improving azimuth resolution as
 363 compared to the unfiltered data in Figure 4A. In effect we reveal and can track during the day
 364 numerous thunderstorm centers at different azimuths with slightly improved resolution. One should
 365 note that, as mentioned above, some thunderstorm activity appears also close to the HT geographic
 366 azimuth of $\approx 33^\circ$ long before the volcano first eruption and the accompanied signal is continuously
 367 observed also during the HT main eruption, which is not visible in this plot with small n and $r_{\min} \gg$
 368 $r_{50\text{Hz}}$. Thus, we interpret here the respective maximum $\approx 33^\circ$ in the azimuths' distribution during the
 369 eruption as the projected local thunderstorm activity, not related to the HT. On the other hand, by
 370 selecting r_{\min} and r_{\max} below the value of $r_{50\text{Hz}}$ one can clearly reveal the signal with azimuths from the
 371 HT first and second eruptions, but with a large scatter. It shows that the applied filtering procedure
 372 cleans nicely the individual high amplitude impulses but is not able to do the same for the low
 373 amplitude fluctuations in the data. At this figure (Fig. 4) one may note the previously discussed
 374 azimuth dependent switching-off of the thunderstorm activity in the morning, finishing in a few cases
 375 with the azimuth distributions' upturns.

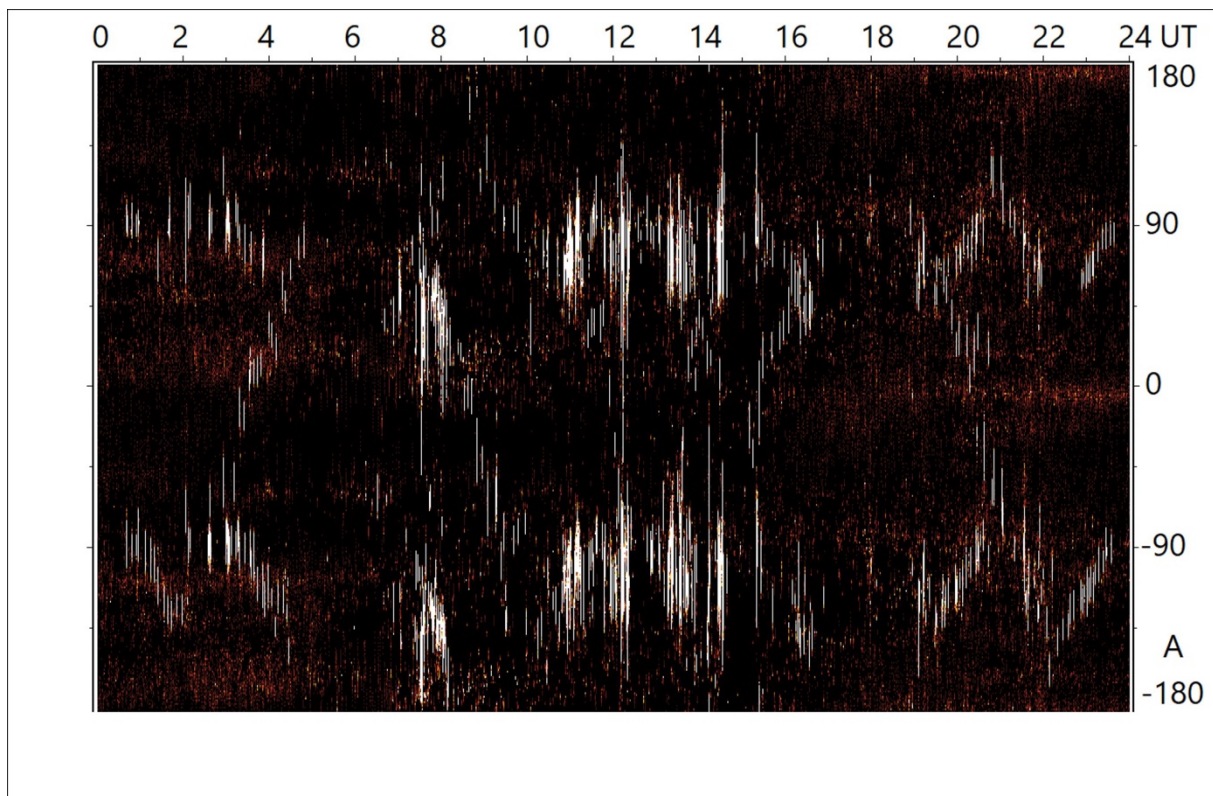
376



377
 378
 379 Figure 5. Comparing daily ELF signal azimuth distributions derived with $n=1$ for the data with filtered
 380 50 Hz line using **A.** the bandstop filter for $r_{\min}=300$ and $r_{\max}=3000$ (upper left); **B.** the MA60 filter for
 381 $r_{\min}=6$ and $r_{\max}=30$ (upper right) and **C.** the bandstop filter for $r_{\min}=6$ and $r_{\max}=30$ (bottom).

382
 383 A quite different output is obtained when using the MA60 filter. In effect, as presented on
 384 Figure 1C, D, the impulses with steep rising and declining slopes are removed or at least highly
 385 attenuated in the filtered data. Thus, only the slowly varying or low amplitude signals are available for
 386 the analysis with a selected n below 60. Let us perform azimuth analysis in such data with $r_{\max} < r_{50\text{Hz}}$.
 387 Example distributions resulting for $n=1$, $r_{\min}=6$ and $r_{\max}=30$ are compared in Figure 5 with the results
 388 for the data cleaned using the bandstop filter. It is important to note that the characteristic azimuth
 389 stripes from thunderstorms visible in this figure for the MA60 filter (Figure 5B) coincide with the
 390 azimuths derived from high amplitude impulses using the bandstop filter (Figure 4B and 5A) as well
 391 as the ones without any filtering for $r_{\min} \gg r_{50\text{Hz}}$ (Figure 4A). Thus, somehow to our surprise the
 392 MA60 filtered data presented in Figure 1D preserved the azimuth information in the slowly varying
 393 signal, including clear signatures from the HT eruption at $A \approx 20^\circ$. It is contrary to slowly varying
 394 signals in the bandstop filtered data providing highly dispersed azimuth distributions in Figure 5C.
 395 One should note that the HT azimuth distribution derived in this analysis matches well to the ones
 396 derived from both the bandstop filtered data and, from the raw data, when using large amplitude
 397 signals with larger n . This fact confirmed consistency of all considered approaches and in the same
 398 time reality of the obtained azimuths.

399 Another interesting case in this analysis can be studying ultra-low frequency magnetospheric
 400 PC fluctuations (see e.g. Kivelson, M.G. and Russell, C.T. 1995), studied earlier in the Hylaty station
 401 by Nieckarz (2016) and Nieckarz & Michalek (2020). To illustrate this possibility, we selected a large
 402 $n=3000$ and -- from the data inspection -- we choose $r_{\min}=10^3$ and $r_{\max}=10^4$ for the analysis to obtain
 403 results presented in Figure 6. It is interesting to note that the registered long wave azimuths are well
 404 constraint to some discrete directions, forming a regular time pattern and revealing clear differences in
 405 the observed trends between waves propagating in the early and late hours of the day, and in the
 406 daytime. We note that on Jan. 15th, 2022, there is lack of such high amplitude waves in time periods of
 407 5-7 UT and 17-18:30 UT, close to the sunrise and the sunset in the Hylaty station (where the local time
 408 = UT + 1h in winter). The measurements of large amplitude short spikes create more diffuse
 409 “background” stripes of colored points at the plot, around azimuths of nearby thunderstorms.
 410



411
 412 Figure 6. Daily signal azimuth distribution derived using 1s ($n=3000$) time step, with $r_{\min}=10^3$ and
 413 $r_{\max}=10^4$ for the non-filtered data. White lines result from long (~ 1 s or longer) high amplitude waves,
 414 while red/yellow points in the background are created by short large lightning spikes in the data.

415

416 5. Conclusions

417

418 In the present study we show that with high quality ELF measurements, like our data from the ELA11
 419 sensor, one can separate ELF signals emitted from numerous thunderstorm regions distributed along
 420 the Earth. This very fact indicates that in many time instants signals from individual thunderstorm

421 regions dominate the measurements. It is contrary to our original expectation that in the majority of
422 observations – with the exception of large impulses - one would register a superposition of signals
423 from sources from a wide range of azimuths

424 To analyze azimuths of the registered ELF signals we proposed a new simple, but powerful
425 method comparing signal changes in two perpendicular magnetic antennas, as presented in Section 3.
426 By selecting 3 parameters in this method, the maximum and minimum signal changes, r_{\max} and r_{\min} ,
427 and the time scale for these changes characterized with n , one can study waves/impulses with different
428 frequencies and amplitudes, to take into account the modification (dispersion) of the signal shape
429 during its propagation in the earth-ionosphere cavity. Thus, by selecting different sets of (r_{\max}, r_{\min}, n)
430 one can study different aspects of the thunderstorms' distribution and its varying activity. The derived
431 azimuths are more precise after one remove interference from the electric grid.

432 In the case of analyzing the signal changes smaller or comparable to the ones from the 50 Hz
433 electric power line perturbations, significant scatter is observed in the derived azimuth distribution. A
434 possibility to take into account such periodic perturbations is to measure the natural ELF signal
435 changes in the same phase of the electric power line signal, by selecting $n=60$ in our data for the
436 respective time delay between measurements. However, as one could see in Figure 1D, the power line
437 signal registered in our Hylaty station is not as regular as we would wish to have and accuracy
438 improvement of azimuth resolution for small measured amplitudes r appears to be quite moderate. On
439 the other hand, the analysis resolves separate thunderstorm directions for large impulses. Overall,
440 usage of $n=60$ falls short of the main intended goal of enabling study of azimuth information of small
441 amplitude ELF impulses.

442 To deal with this problem we tested the filtering of the 50 Hz signal from the data with two
443 significantly different filtering procedures. The bandstop filtering appears excellent in "cleaning" steep
444 impulses/spikes in the ELF signal and providing a significant improvement for derived azimuths. The
445 procedure decreases dispersion of azimuths derived for high amplitude impulses and it enables
446 reasonable thunderstorm direction resolution using even smaller spikes. Unfortunately, the small
447 amplitude waves in such filtered signal do not show clear azimuth separation, possibly due to
448 remaining perturbations left from the wide and thus not fully removed wings of the 50 Hz line.

449 When inspecting Figure 1D, at first glance the results of the applied low pass MA60 filter does
450 not give much hope for extracting detailed directional information about numerous thunderstorms.
451 However, despite the removal/deformation of the quickly varying impulses, this signal still contains
452 quite precise information about waves propagating from many different azimuths, also when analyzing
453 low amplitude signal changes with $r \ll r_{50\text{Hz}}$. Apparently, short impulses in both antennas are corrected
454 in the same proportion, without a noticeable change of the azimuth values resulting from equation 1.
455 Studying of such low amplitude or slowly varying signals is essential in identifying emissions from
456 distant sources, with impulses smoothed due to large dispersions.

457 A fortunate (for ELF research!) strong and extended in time point-like electromagnetic
458 emission from the HT eruption allowed us to analyze the propagation of ELF waves along a trajectory
459 crossing the Earth polar region and to test our azimuth derivation method for extracting a particular
460 source signal from the general electromagnetic activity in the earth-ionosphere cavity. The long >16
461 Mm direct propagation path introduces significant dispersion into the volcano lightnings' generated
462 spikes. In effect, the HT azimuth signal is clearly visible when limiting analysis to the slowly varying
463 signals, while analysis of high amplitude and fast changing impulses does not show any clear HT
464 signature. Moreover, in this last case one can monitor in the azimuth distribution evolution map the
465 thunderstorm signals from directions close to the HT geographic azimuth, which are overshadowed in
466 the lower amplitude measurements by a dominating HT contribution. The analysis also shows the
467 research potential of azimuths distribution studies, by allowing a robust identification of the weaker
468 secondary HT eruption. The method allows for precise measurement of the significant (>10°) HT ELF
469 signal azimuth deviation from the geographic azimuth due to wave deflection in the polar region
470 and/or the waves propagation near the solar terminator, in the process discussed earlier by Mlynarczyk
471 et al. (2017).

472

473 **Acknowledgements**

474

475 Authors are grateful to Astronomical Observatory of the Jagiellonian University for continues support
476 of ELF research and operation of the WERA magnetic sensors' array. The development of ELA11
477 sensor has been supported by the National Science Centre, Poland, under Grant
478 2015/19/B/ST10/01055. This research was partly funded by the National Science Centre, Poland, grant
479 2023/49/B/ST9/02777. Mark Golkowski was supported by National Science Foundation Award AGS
480 2312282 to University of Colorado Denver. The authors are grateful to Alexander Nickolaenko and
481 two anonymous referees for critical remarks and valuable advice helping to improve the manuscript.

482

483 **Open research**

484

485 The data analyzed in the present paper are available from an on-line repository (Kubisz 2023).

486

487 **References**

488

489 Bor, J., Bozoki, T., Satori, G., Williams, E., Behnke, et al. 2023. Responses of the AC/DC global
490 electric circuit to volcanic electrical activity in the Hunga Tonga-Hunga Ha'apai eruption on 15
491 January 2022. *Journal of Geophysical Research: Atmospheres*, **128**, e2022JD038238.
492 <https://doi.org/10.1029/2022JD038238>

493

494 Coughlin, M. W., Cirone, A., Meyers, P., Atsuta, S., Boschi, et al. 2018. Measurement and subtraction
495 of Schumann resonances at gravitational-wave interferometers. *Physical Review D*, **97**(10), 102007.
496 <https://doi.org/10.1103/PhysRevD.97.102007>

497

- 498 Füllekrug, M., Sukhorukov, A. I. 1999. The contribution of anisotropic conductivity in the ionosphere
 499 to lightning flash bearing deviations in the ELF/ULF range. *Geophysical Research Letters*, **26**(8),
 500 1109-1112. <https://doi.org/10.1029/1999GL900174>
 501
- 502 Füllekrug, M., Constable, S. 2000. Global triangulation of intense lightning discharges. *Geophysical*
 503 *Research Letters*, **27**(3), 333-336. <https://doi.org/10.1029/1999GL003684>
 504
- 505 Gołkowski, M., Inan, U. S. 2008. Multistation observations of ELF/VLF whistler mode chorus,
 506 *Journal of Geophysical Research*, **113**, A08210, doi:10.1029/2007JA012977.
 507
- 508 Gołkowski, M., Sarker, S. R., Renick, C., Moore, R. C., Cohen, et al. 2018. Ionospheric D
 509 region remote sensing using ELF sferic group velocity. *Geophysical Research Letters*, **45**(23),
 510 12-739. <https://doi.org/10.1029/2018GL080108>
 511
- 512 Hosseini, P., Gołkowski, M., Chorsi, H. T., Gedney, S. D., Moore, R. C. 2018. Using eccentricity to
 513 locate ionospheric exit points of magnetospheric whistler mode waves. *IEEE Transactions on*
 514 *Geoscience and Remote Sensing*, **56**(12), 7049-7061. doi: [10.1109/TGRS.2018.2847605](https://doi.org/10.1109/TGRS.2018.2847605)
 515
- 516 Jones, D. L., & Kemp, D. T. (1971). The nature and average magnitude of the sources of transient
 517 excitation of Schumann resonances. *Journal of Atmospheric and Terrestrial Physics*, **33**(4), 557-566.
 518
- 519 Kemp, D. T. (1971), The global location of large lightning discharges from single station observations
 520 of elf disturbances in the Earth-ionosphere cavity, *J. Atmos. Terr. Phys.*, **33**, 919–927,
 521 doi:10.1016/0021-9169(71)90091-2.
 522
- 523 Kemp, D. T., and D. Llanwyn Jones (1971), A new technique for the analysis of transient ELF
 524 electromagnetic disturbances within the Earth-ionosphere cavity, *J. Atmos. Terr. Phys.*, **33**, 567–572.
 525
- 526 Kivelson, M.G. and Russell, C.T. (1995). Introduction to Space Physics, *Cambridge University Press*,
 527 p. 330. ISBN 9780521457149.
 528
- 529 Kubisz, J. 2023 [Dataset] A set of measurement data from the ELA11 magnetometer from January 15,
 530 2022, Hylaty Station, Poland
 531 <https://uj.rodruk.pl/dataset.xhtml?persistentId=doi:10.57903/UJ/NSRSLE>
 532
- 533 Kulak, A., Kubisz, J., Klucjasz, S., Michalec, A., Mlynarczyk, J., et al. 2014. Extremely low frequency
 534 electromagnetic field measurements at the Hylaty station and methodology of signal analysis. *Radio*
 535 *Science*, **49**, 361–370. <https://doi.org/10.1002/2014RS005400>
 536
- 537 Mezentssev, A., Nickolaenko, A. P., Shvets, A. V., Galuk, Yu. P., Schekotov, A. Yu., Hayakawa, M.,
 538 Romero, R., Izutsu, J., Kudintseva, I. G. 2022. Observational and model impact of Tonga volcano
 539 eruption on Schumann resonance, *Journal of Geophysical Research: Atmospheres*, **128**,
 540 e2022JD037841. <https://doi.org/10.1029/2022JD037841>
 541
- 542 Mitchell, V. B. 1976. Schumann resonance—some properties of discrete events, *Journal of Atmospheric*
 543 *and Solar-Terrestrial Physics*, **38**, 77–82
 544
- 545 Mlynarczyk, J., Kulak, A., Salvador, J. 2017. The accuracy of radio direction finding in the extremely
 546 low frequency range. *Radio Science*, **52**(10), 1245-1252. <https://doi.org/10.1002/2017RS006370>
 547
- 548 Nickolaenko, A. P. 1997. Modern aspects of Schumann resonance studies. *Journal of Atmospheric and*
 549 *Solar-Terrestrial Physics*, **59**(7), 805-816. [https://doi.org/10.1016/S1364-6826\(96\)00059-4](https://doi.org/10.1016/S1364-6826(96)00059-4)
 550

- 551 Nickolaenko, A. P., Hayakawa, M. 2002. Resonances in the Earth-ionosphere cavity. Vol. **19**. *Springer*
 552 *Science & Business Media*.
 553
- 554 Nickolaenko, A. P., Galuk, Yu P. Hayakawa, M., 2018. Deviations of source bearing in the Earth–
 555 ionosphere cavity with the day-night non-uniformity. *Telecommunications and Radio Engineering*,
 556 **77**(11), 995-1016 DOI: 10.1615/TelecomRadEng.v77.i11.50
 557
- 558 Nickolaenko, A. P., Galuk, Yu P. Hayakawa, M., Kudintseva, I. G. 2021. Model source
 559 bearings of Q-bursts for observations in Antarctica, *Journal of Atmospheric and Solar-*
 560 *Terrestrial Physics*, **222**, 105723. <https://doi.org/10.1016/j.jastp.2021.105723>
 561
- 562 Nickolaenko, A. P., Schekotov, A. Y., Hayakawa, M., Romero, R., Izutsu, J. 2022. Electromagnetic
 563 manifestations of Tonga eruption in Schumann resonance band. *Journal of Atmospheric and Solar-*
 564 *Terrestrial Physics*, **237**, 105897. <https://doi.org/10.1016/j.jastp.2022.105897>
 565
- 566 Nickolaenko, A. P., Sentman, D. D. 2007, Line splitting in the Schumann resonance oscillations, *Radio*
 567 *Science*, **42**, RS2S13. <https://doi.org/10.1029/2006RS003473>
 568
- 569 Nickolaenko, A. P., Shvets, A.V., Galuk, Yu.P., Schekotov, A. Y., Hayakawa, M., et al. 2023. Power
 570 flux in the Schumann resonance band linked to the eruption of Tonga volcano on Jan. 15, 2022. (Two
 571 point measurements of Umov-Poynting vector). *Journal of Atmospheric and Solar-Terrestrial Physics*,
 572 **247**, 106078. <https://doi.org/10.1016/j.jastp.2023.106078>
 573
- 574 Nieckarz, Z. (2016). Imprints of Natural Phenomena and Human Activity Observed During 10 Years
 575 of ELF Magnetic Measurements at the Hylaty Geophysical Station in Poland, *Acta Geophysica* **64**,
 576 2591-2608. DOI: 10.1515/acgeo-2016-01
 577
- 578 Nieckarz, Z., Kulak, A., Zieba, S., Odzimek, A. (2011), Cloud-to-ground lightning dipole moment
 579 from simultaneous observations by ELF receiver and combined direction finding and time-of-arrival
 580 lightning detection system, *Journal of Geophysical Research*, **116**, D08107.
 581 doi:10.1029/2010JD014736.
 582
- 583 Nieckarz, Z. and Michałek, G. (2020). Long-term observation of magnetic pulsations through the ELF
 584 Hylaty station located in the Bieszczady Mountains (south–eastern Poland), *J. Space Weather Space*
 585 *Clim.* **10**, 59. <https://doi.org/10.1051/swsc/2020063>
 586
- 587 Price, C. 2016. ELF electromagnetic waves from lightning: The Schumann resonances. *Atmosphere*,
 588 **7**(9), 116. <https://doi.org/10.3390/atmos7090116>
 589
- 590 Shvets, A.V., Nickolaenko, A.P., Koloskov, A.V., Yampolsky, Y.M., Budanov, et al. 2022. Day
 591 after day variations of arrival angles and polarisation parameters of Q bursts recorded at
 592 Antarctic station “Akademik Vernadsky”, *Journal of Atmospheric and Solar-Terrestrial*
 593 *Physics*, **229**, 10581. <https://doi.org/10.1016/j.jastp.2021.105811>
 594
- 595 Strangeways, H. J., Rycroft, M.J. 1980, Systematic errors in VLF direction-finding of whistler ducts—
 596 II, *Journal of Atmospheric and Solar-Terrestrial Physics*, **42**, 1009– 1023.
 597 [https://doi.org/10.1016/0021-9169\(80\)90114-2](https://doi.org/10.1016/0021-9169(80)90114-2)
 598
- 599 Wood, T. G., Inan U. S. 2002. Long-range tracking of thunderstorms using sferic measurements,
 600 *Journal of Geophysical Research*, **107**(D21), 4553, doi:10.1029/2001JD002008.
 601

602 Wood, T. G., Inan U. S. 2004. Localization of individual lightning discharges via directional and
603 temporal triangulation of spheric measurements at two distant sites, Journal of Geophysical Research,
604 **109**, D21109, doi:10.1029/2004JD005204.
605